

Bimodal Resonance Phenomena—Part II: High/Low-Contrast Grating Resonators

*Original*

Bimodal Resonance Phenomena—Part II: High/Low-Contrast Grating Resonators / Orta, Renato; Tibaldi, Alberto; Debernardi, Pierluigi. - In: IEEE JOURNAL OF QUANTUM ELECTRONICS. - ISSN 0018-9197. - 52:12(2016), pp. 1-8. [10.1109/JQE.2016.2623272]

*Availability:*

This version is available at: 11583/2657917 since: 2018-11-08T11:10:08Z

*Publisher:*

IEEE

*Published*

DOI:10.1109/JQE.2016.2623272

*Terms of use:*

This article is made available under terms and conditions as specified in the corresponding bibliographic description in the repository

*Publisher copyright*

IEEE postprint/Author's Accepted Manuscript

©2016 IEEE. Personal use of this material is permitted. Permission from IEEE must be obtained for all other uses, in any current or future media, including reprinting/republishing this material for advertising or promotional purposes, creating new collecting works, for resale or lists, or reuse of any copyrighted component of this work in other works.

(Article begins on next page)

# Bimodal Resonance Phenomena. Part II: High/Low-Contrast Grating Resonators

Renato Orta, *Senior Member, IEEE*, Alberto Tibaldi, and Pierluigi Debernardi

**Abstract**—Several groups are currently working on integrated optical resonators. In this context, one of the most interesting implementations is based on high-contrast gratings, featuring high- $Q$  Fano resonances. Mastering these phenomena can potentially open up the possibility to exploit such devices for the implementation of vertical-coupled filters or compact monolithic lasers. To this aim, in this paper the novel analytic framework introduced in Part I is applied to complement the design guidelines present in the literature. Through explicit expressions of the loop gain eigenvalues it is possible to predict the positions and quality factors of resonances in crossing and anticrossing points. Moreover, a quantitative connection between these points and Fano resonances is established. The framework presented in this paper has been useful for identifying, in a low-contrast grating, resonance features similar to those well known in high-contrast structures.

**Index Terms**—Gratings, dielectric resonators, coupled mode analysis

## I. INTRODUCTION

RESONATORS are key blocks in a vast multitude of applications in electronics, microwaves, optics and several other subjects. Focusing the discussion on optics, several implementations of resonators exhibiting a high quality factor ( $Q$ ) have been attempted based on microrings [1], photonic crystals [2] and gratings, such as the cavity resonator integrated guided-mode-resonance filter (CRIGF) [3], [4]. A very interesting possibility relies on high-contrast gratings (HCGs). Apart from their most popular application as ultrabroadband reflectors [5], attention has been given to their resonance features, with particular emphasis on the presence of Fano resonances in their reflectivity spectra [6]–[10]. This topic is currently inspiring several research groups, leading to remarkable proposals such as the hybrid grating [11]. Furthermore, in view of performing an extreme miniaturization of solid state light sources, the realization of a vertical-cavity surface-emitting laser (VCSEL) obtained simply by introducing active material in the HCG bars, without additional mirrors, would be a major breakthrough [6].

The aim of this paper is to advance into the study of HCG resonators and their working principles. The first part of this series of papers [12] provides a theoretical model suitable for the study of HCGs, viewed as bimodal Fabry-Pérot

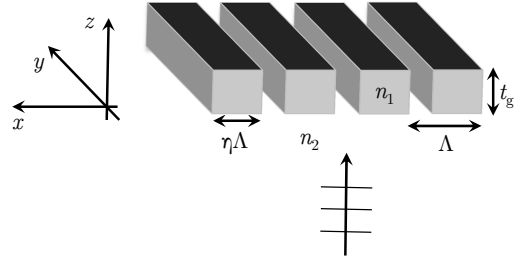


Fig. 1. Sketch of the high-contrast grating geometry, where the relevant parameters are indicated.

interferometers. In this second part, that parametric framework is exploited to quantify the relationships between resonances and transmission/reflection peaks, which have been observed by the group of C. Chang-Hasnain [6]–[10]. They provided design guidelines for HCG resonators inspired by an analogy between their resonance curves and coupled-mode theory. In Section II their results are reinterpreted in our framework and reproduced with the parametric model described in Part I, so as to highlight the strong connections between the resonance and reflectivity HCG features. Explicit expressions of the loop gain eigenvalues are provided in Section III. A complete, rigorous characterization of crossing and anticrossing points is reported: their existence conditions and positions are derived, providing explicit expressions of the resonance  $Q$  factor. Moreover, their relationship with Fano resonances and leaky waves is discussed. The possibility to easily explore the model parameter space suggested us to exploit low-contrast gratings as alternative high- $Q$  resonators, as described in Section IV.

## II. A REVIEW OF HCG RESONATORS

The geometry of a high-contrast grating (HCG) is sketched in Fig. 1. This consists of an array of dielectric bars with refractive index  $n_1$  surrounded by a medium with much lower index  $n_2$  (commonly, air), uniform along  $y$ , having period  $\Lambda$  along  $x$  and thickness  $t_g$  along  $z$ . The duty cycle  $\eta$  is defined as the ratio of the widths (along  $x$ ) of the high refractive index portion to the period. HCGs are operating in the near-wavelength regime, where the approximations applicable to gratings for very narrow or very large periods cannot be applied; more in detail, the HCG operating range is characterized by having one propagating plane-wave in the half-spaces surrounding the bars and two modes in the grating region, so that full-wave simulators such as the ones based

R. Orta is with the Department of Electronics and Telecommunications, Politecnico di Torino, Turin, 10129 Italy, and with IEIIT-CNR; e-mail: renato.orta@polito.it

A. Tibaldi and P. Debernardi are with the Consiglio Nazionale delle Ricerche (CNR), Istituto di Elettronica e di Ingegneria dell'Informazione e delle Telecomunicazioni (IEIIT), 10129 Turin, Italy.

Manuscript received August 2, 2016; revised October 14, 2016; accepted October 18, 2016.

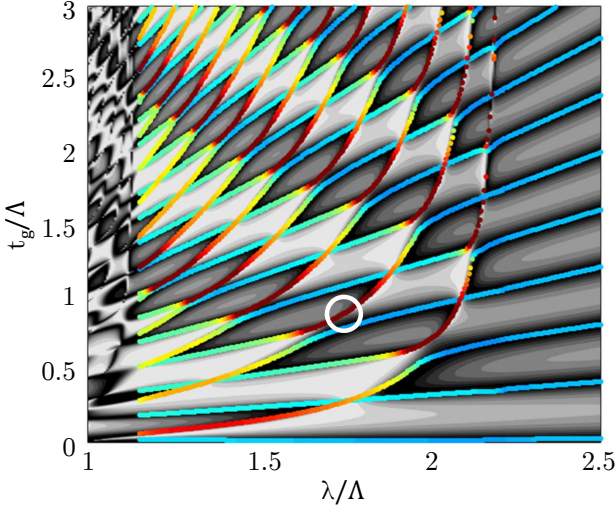


Fig. 2. TE reflectivity map for normal-incident plane-wave (linear, gray scale: brighter regions indicate high reflectivity) of a HCG in the  $(\lambda, t_g)$  plane. The grating consists of bars with  $n_1 = 3.48$  surrounded by air,  $\eta = 60\%$ , from [10, Fig. 6(b)]. The resonance curves are superimposed and their color quantifies the resonance quality factor (blue low, red high). The marker indicates the point  $P$  ( $\lambda = 1.722\Lambda$ ,  $t_g = 0.8507\Lambda$ ), where  $Q \rightarrow \infty$ .

on the rigorous coupled wave analysis (RCWA) are necessary [13]-[15].

Design guidelines for resonators based on HCGs have been proposed in the literature as results of a numerical parametric study [10], as shown for example in Fig. 2. This reports the normal-incidence plane-wave reflectivity map for the TE polarization in the  $(t_g, \lambda)$  plane, normalized to the grating period  $\Lambda$ , obtained by means of the RCWA with  $N_m = 11$  Floquet modes. Even if the map is produced for a larger band, the region of interest is that where only one plane-wave is propagating outside the grating and two modes are above cutoff in the internal region, *i.e.*  $\lambda \in [1.2, 2]\Lambda$ . Indeed, this corresponds to the HCG operation band, for which the parametric model described in Part I has been developed.

Standard (single mode) Fabry-Pérot interferometers (FPIs) exhibit resonances (transmission peaks) when the round-trip phase shift (RTPS) is an integer multiple of  $2\pi$ . In the case of a bimodal cavity there are two RTPSs associated with the two oscillation eigenmodes, defined in terms of the eigenvectors of the loop gain matrix, and their role in determining the cavity response is not obvious at first sight. Since the HCG under study is symmetric, as proposed by [10] it is convenient to study the half loop gain matrix

$$\mathbf{T}_{\frac{1}{2}} = \mathbf{E} \bar{\mathbf{S}}_{ii}'' \mathbf{E}. \quad (1)$$

Here,  $\bar{\mathbf{S}}_{ii}''$  is the generalized reflection coefficient of the bar-air junction seen from the inner region.  $\mathbf{E}$  is the reference plane shift matrix from the junction to the center of the bars, defined in [12].

Superimposed on the map of Fig. 2 is a set of lines, which from now on will be referred to as “resonance curves”, indicating when the RTPSs of the eigenmodes (related to the squares of the eigenvalues of  $\mathbf{T}_{\frac{1}{2}}$ ) equal a multiple of  $2\pi$ . These curves appear to be closely related to the reflectivity map. Moreover, it

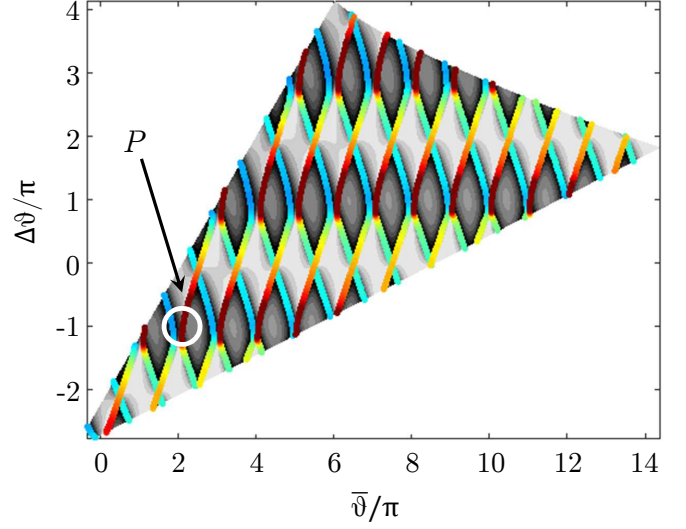


Fig. 3. Same reflectivity map of Figure 2, redrawn in the  $(\bar{\vartheta}, \Delta\vartheta)$  plane with reference to the dual-mode region  $\lambda \in [1.2, 2.0]\Lambda$ . The marker indicates the image of the point  $P$  of Fig. 2.

can be noted that the curves can intersect or repel each other, resulting in the so-called “crossing points” or “anticrossing regions”. The crossing occurs between resonance curves corresponding to half round trip phase shift (HRTPS=RTPS/2) differing by  $\pi$ . The curves corresponding to HRTPS differing by 0 or  $2\pi$  give rise to anticrossings. Particular attention has been dedicated to the latter, since the guidelines proposed in [10] suggest to design high- $Q$  HCG resonators in such regions. The different behavior between crossings and anticrossings was attributed to absence or existence of coupling, due to the similarity of these curves to the ones describing the dispersion relation in coupled-mode theory. The presence of high- $Q$  regions can be observed in Fig. 2 by referring to the color scale of the resonance curves, which qualitatively show the corresponding  $Q$  factor.

This map will be interpreted in the following sections by means of the bimodal Fabry-Pérot interferometer (FPI) model described in Part I, taking advantage of the introduced parametrization and of the consequent analytic expressions. As a first step, the dual-mode operation rectangle of Fig. 2 is transformed into Fig. 3, by exploiting the change of variables

$$\bar{\vartheta} = \frac{k_{z1} + k_{z2}}{2} t_g + \varphi_c \quad \Delta\vartheta = (k_{z1} - k_{z2}) t_g + 2\Delta, \quad (2)$$

where  $\varphi_c$  and  $\Delta$  are parameters of the junction scattering matrix, evaluated at each wavelength. It can be immediately noted that the considered portion of the  $(\lambda, t_g)$  plane is mapped into a sort of “pizza slice”, where the long sides are straight segments. In fact, they are the image of the rectangle vertical sides  $\lambda = 1.2\Lambda$  and  $\lambda = 2\Lambda$ : the variation of  $t_g$  causes a proportional variation of both  $\bar{\vartheta}$  and  $\Delta\vartheta$  in (2). Instead, the short side is quite similar to a hyperbola, just like the dispersion curves of the grating mode propagation constants  $k_{z1}$  and  $k_{z2}$ . The  $(\bar{\vartheta}, \Delta\vartheta)$  plane appears to be a better framework for the representation of crossing/anticrossing states, since

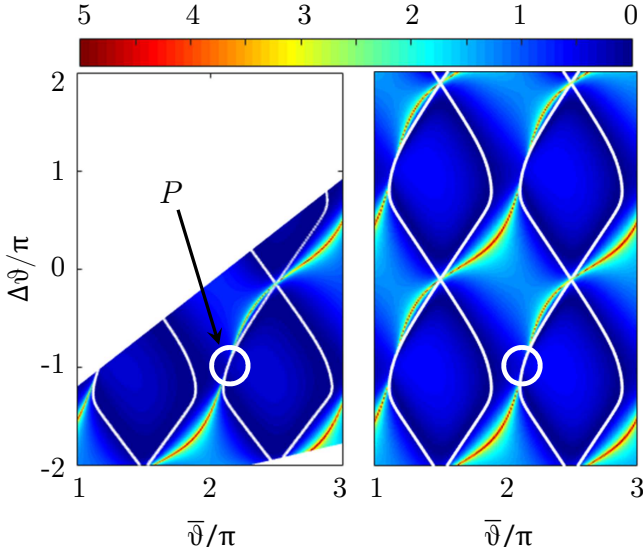


Fig. 4. Reflectivity map in number of nines (see text) of the bimodal FPI. Left: detail of Fig. 3 expressed in number of nines. Right: analytic result with junction parameters  $\Theta = 62.55^\circ$ ,  $\Phi = 33.26^\circ$ ,  $\Psi = 246.02^\circ$  evaluated at point  $P$ . The white lines are the resonance curves. Red indicates reflectivity higher than 99.999%. The marker indicates the image of the point  $P$  of Fig. 2 in the transformed coordinate system,  $\bar{\vartheta}/\pi = 2.13$ ,  $\Delta\vartheta/\pi = -1$ .

the resonance curves are straightened, assuming an almost sinusoidal behavior in  $\Delta\vartheta$ .

Focusing on an anticrossing region, (operating point  $P$ :  $\lambda = 1.722\Lambda$ ,  $t_g = 0.8507\Lambda$ , where  $Q \rightarrow \infty$ ), the scattering matrix of the bar-air interface has been computed by the RCWA in the point  $P$  only. Then, its parametrization is obtained from [12, eq. (28)], and the formulation described in Part I is applied to produce the results shown in Fig. 4(right). In Fig. 4(left) a zoom of the reflectivity map of Fig. 3 is reported for comparison. The reflectivities are reported in number of nines  $R^{(\#9)} = -\log_{10}(|S_{21}|^2)$ , emphasizing a locus of points where reflectivity is greater than 99.999% (red lines). The white lines indicate the resonance curves; they are reported also in Fig. 5(left) for the same structure. It should be noted that even if the model is accurate in the neighborhood of the specified point  $P$ , there is a good agreement between the two plots in Fig. 4 also far from it, proving its validity also if dispersion is neglected. The map in Fig. 4(right) is obtained with the explicit expression [12, eq. (24)]. The high- $Q$  region corresponds to the tangency of the white and red lines (see Fig. 5, point  $F$ ), but cannot be appreciated for graphical reasons. It is to be remarked once more that the map in Fig. 4(right) has been computed by means of a single RCWA computation.

### III. PARAMETRIC STUDY OF THE LOOP GAIN EIGENVALUES

The model proposed in Part I is now applied to characterize the HCG resonance properties. To this aim, the parametrization of the junction scattering matrix is exploited to write the elements of the half loop gain matrix (1)

$$\begin{aligned} (\mathbf{T}_{\frac{1}{2}})_{11} &= (\cos^2 \Phi \cos \Theta e^{j\Psi} - \sin^2 \Phi e^{-j\Psi}) e^{-j\Delta\vartheta/2} \\ (\mathbf{T}_{\frac{1}{2}})_{12} &= (\mathbf{T}_{\frac{1}{2}})_{21} = j \frac{1}{2} \sin 2\Phi (\cos \Theta e^{j\Psi} + e^{-j\Psi}) \\ (\mathbf{T}_{\frac{1}{2}})_{22} &= (-\sin^2 \Phi \cos \Theta e^{j\Psi} + \cos^2 \Phi e^{-j\Psi}) e^{j\Delta\vartheta/2}. \end{aligned} \quad (3)$$

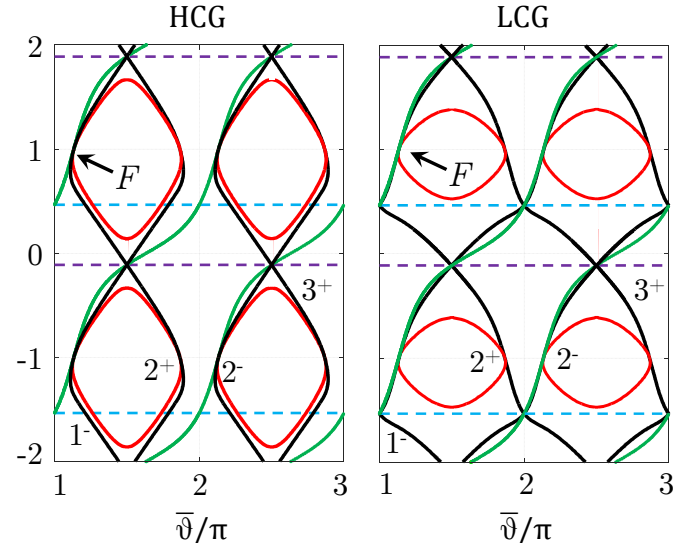


Fig. 5. Curves representing the loci of the transmission zeros  $\bar{\vartheta}_{z,21}$  (green), of the real reflection zeros  $\bar{\vartheta}_{z,11}$  (red), and the resonance curves (black), labeled by the relevant mode indexes, see (17). The horizontal dashed lines indicate the positions of crossing points (purple) and of real trace of the half loop gain matrix (blue). Left: structure analyzed in Fig. 4. Right: structure with  $\Theta = 83.00^\circ$ ,  $\Phi = 33.26^\circ$ ,  $\Psi = 246.02^\circ$ , relative to a low-contrast grating. The three curves are tangent in the point  $F$ .

Then, explicit expressions of the half loop gain eigenvalues  $\lambda_i$  can be derived as the roots of the characteristic polynomial

$$\lambda^2 - 2t\lambda + d = 0, \quad (4)$$

which can be expressed in terms of the half-trace  $t$  and of the determinant  $d$  of  $\mathbf{T}_{\frac{1}{2}}$

$$\lambda_i = t \pm \sqrt{t^2 - d}, \quad (5)$$

where  $d = \lambda_1 \lambda_2 = \cos \Theta$ . Notice a remarkable result of this analysis: the product of the magnitudes of the loop gain eigenvalues equals  $|\bar{S}_{33}|^2$ , *i.e.* the reflectivity of the grating interface (see [12, eq. (20)]).

In order to explain the shape of the resonance curves depicted in Fig. 4, the half-trace  $t$  is conveniently written as

$$t = \frac{c^-}{2} e^{-j\Delta\vartheta/2} + \frac{c^+}{2} e^{j\Delta\vartheta/2}, \quad (6)$$

with  $c^-$ ,  $c^+$  following from (3).

Figure 6(left) shows the trajectories  $\lambda_i(\Delta\vartheta)$  in the complex plane for the  $\Theta$ ,  $\Phi$ ,  $\Psi$  values used in Fig. 4; the center and right plots have been obtained with larger values of  $\Theta$  corresponding to less reflecting junctions (see [12, eq. (20)]), *i.e.* lower grating duty cycle or bar refractive index. In other words, this plot refers to a low-contrast grating (LCG). The eigenvalues trace closed trajectories that may or may not contain the origin. In Fig. 6(center), the curves meet in two points on the real axis and the eigenvalues are actually coincident for the  $\Delta\vartheta$  values given by (13). This configuration is the element of separation between the left and right cases. It is to be remarked that the curves exhibit always a point of tangency to the unit circle, for any choice of the junction parameters, so that  $Q \rightarrow \infty$  in that point. To obtain explicit expressions of the various

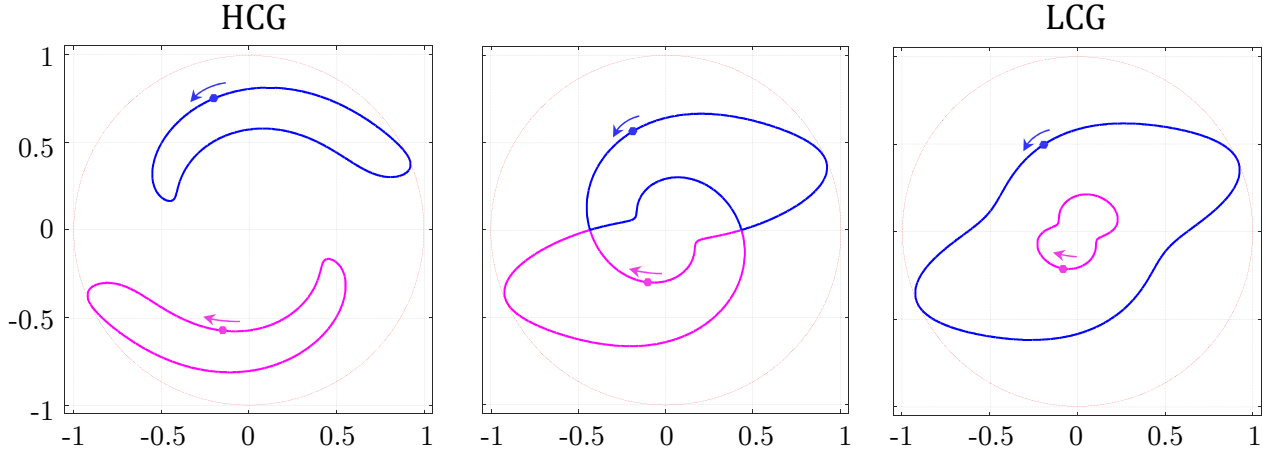


Fig. 6. Parametric study of the half loop gain eigenvalues  $\lambda_i(\Delta\vartheta)$  for  $\Phi = 33.26^\circ$ ,  $\Psi = 246.02^\circ$  (as in Fig. 4) and  $\Delta\vartheta \in [0, 4\pi]$ . The left, center and right figures refer to  $\Theta = 62.55^\circ$  (corresponding to a HCG),  $\Theta = \Theta_c = 79.15^\circ$  (obtained from (15)),  $\Theta = 83.00^\circ$  (corresponding to a LCG). The blue and magenta curves are the orbits of the two eigenvalues in the complex plane. The points mark the  $\Delta\vartheta = 10.00^\circ$  position and the arrows indicate the direction of motion for increasing  $\Delta\vartheta$ . Note that in all cases the trajectories are tangent to the unit circle, drawn in red.

configurations of interest, we chose  $\Psi$  as running variable, so that (6) is rewritten as

$$t = \frac{1}{2}|C| e^{j(\Psi+\arg(C))} + \frac{1}{2\cos\Theta}|C| e^{-j(\Psi+\arg(C))}, \quad (7)$$

with

$$C = \cos\Theta \left( \cos\frac{\Delta\vartheta}{2} \cos 2\Phi - j \sin\frac{\Delta\vartheta}{2} \right).$$

The magnitude and phase of  $C$  are

$$|C| = \cos\Theta \sqrt{1-u^2} \quad \arg(C) = -\arctan v, \quad (8)$$

where the auxiliary variables  $u$  and  $v$  have been defined as

$$\begin{aligned} u &= \sin 2\Phi \cos(\Delta\vartheta/2) \\ v &= \frac{\tan(\Delta\vartheta/2)}{\cos 2\Phi}. \end{aligned} \quad (9)$$

Using (7), it is easily shown that the plot of the discriminant of (4) is an ellipse (symmetrical with respect to the real axis) parametrized by  $\Psi$  that may or may not contain the origin. In particular, if

$$\Theta = \Theta_c = \arccos\left(\frac{1-|u|}{1+|u|}\right), \quad (10)$$

the ellipse passes through the origin for

$$\Psi = \arctan v. \quad (11)$$

This means that if the relations (10) and (11) among  $\Theta$ ,  $\Phi$ ,  $\Psi$  and  $\Delta\vartheta$  hold, then the eigenvalues are coincident. We can now apply these findings to the problem concerning  $\lambda_i(\Delta\vartheta)$ : it is just a matter of eliminating  $\Delta\vartheta$  from the previous expressions so that only  $\Theta$ ,  $\Phi$  and  $\Psi$  appear. Indeed, by inverting (10), it can be found

$$|u| = \tan^2 \frac{\Theta_c}{2}. \quad (12)$$

Then, from (9) and (11),

$$\tan \frac{\Delta\vartheta}{2} = \cos 2\Phi \tan \Psi. \quad (13)$$

Furthermore, from (9)

$$|u| = \sin 2\Phi \left| \cos \frac{\Delta\vartheta}{2} \right| = \frac{\sin 2\Phi}{\sqrt{1 + \tan^2(\Delta\vartheta/2)}}. \quad (14)$$

Finally, from (12)-(14), the touching condition for the trajectories of  $\lambda_i(\Delta\vartheta)$  can be written as

$$\frac{\sin 2\Phi}{\sqrt{1 + \cos^2 2\Phi \tan^2 \Psi}} = \tan^2 \frac{\Theta_c}{2}, \quad (15)$$

which is

$$\tan \Psi = \frac{\sqrt{\sin^2 2\Phi - \tan^4 \frac{\Theta_c}{2}}}{\tan^2 \frac{\Theta_c}{2} \cos 2\Phi}, \quad (16)$$

plotted in Fig. 7 for the values  $\Theta = 62.55^\circ$  and  $\Theta = 83.00^\circ$  (red and green curves). In this  $(\Psi, \Phi)$  parameter plane, each point corresponds to a different grating. For points internal to the region bounded by this contour, the eigenvalues  $\lambda_i(\Delta\vartheta)$  trace two loops not containing the origin, whereas external points correspond to concentric loops (see Fig. 6 (left) and (right) respectively). Finally, if the point lies on the contour, the trajectories have two contact points on the real axis and the eigenvalues are actually coincident in one of them when  $\Delta\vartheta$  has the value given by (13). A marker indicates the operating point  $P$  studied in Fig. 4.

It is to be recalled that  $\mathbf{T}_{\frac{1}{2}}$  is only the  $\bar{\vartheta}$ -independent part of the half loop gain, see [12, eq. (9)]. Note also that the phases of the eigenvalues  $\lambda_i$  are opposite (the determinant of  $\mathbf{T}_{\frac{1}{2}}$  is real positive). Hence, if we call  $n^+$  ( $n^-$ ) the oscillation mode with  $\text{HRTPS}=\bar{\vartheta} + |\arg(\lambda)|$  ( $\text{HRTPS}=\bar{\vartheta} - |\arg(\lambda)|$ ), the resonance curves  $\text{HRTPS}=n\pi$  have the explicit expressions

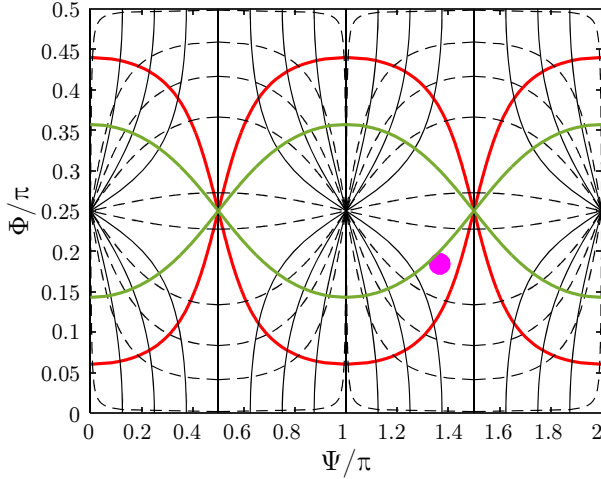


Fig. 7. Parameter plane  $(\Psi, \Phi)$ . The marker indicates the device analyzed in Fig. 4. The thick lines, obtained from (16) for  $\Theta = 62.55^\circ$  (red) and  $\Theta = 83.00^\circ$  (green), indicate the conditions for touching orbits. The contours of constant  $\Delta\vartheta$  (solid, from (18)) and constant  $u$  (dashed, from (21)) of the crossing points are explained in the text.

$$\begin{aligned} \bar{\vartheta}_{n^+} &= n\pi - |\arg(\lambda(\Delta\vartheta))| \quad \text{for mode } n^+ \\ \bar{\vartheta}_{n^-} &= n\pi + |\arg(\lambda(\Delta\vartheta))| \quad \text{for mode } n^-. \end{aligned} \quad (17)$$

These resonance curves are plotted in black in Fig. 5(left) for the parameters of Fig. 4. In order to emphasize the relationship between the reflection and resonance features of the HCG, Fig. 5 reports also the loci of the real zeros of  $S_{11}$  (red, from [12, eq. (26)]), of  $S_{21}$  (green, from [12, eq. (25)]). Note that the zero transmission curves perfectly agree with the high reflectivity regions in Fig. 4.

Figure 5 (right) has been obtained with a larger value of  $\Theta$ , such that no anticrossing regions appear (LCG case). In fact, in Fig. 7 this  $\Theta$  value gives rise to a rather small region bounded by the green contour, such that the marker lies outside of it. By referring to Fig. 6 one can understand the difference in the shape of the resonance curves. In particular, the left panel shows eigenvalues with a phase ranging between a minimum and a maximum. This produces a true anticrossing, with resonance curves in Fig. 5 belonging to modes  $2^+, 2^-$  and  $1^-, 3^+$  approaching up to a point and then separating again. The right panel shows eigenvalues with phases increasing without limits and this gives rise to the transformation of anticrossing points into crossings.

These notions can be now applied to characterize crossing and anticrossing points, their existence conditions and their positions.

#### A. Crossing points

With reference to [10] and (17), crossing points are intersections at  $\bar{\vartheta} = (n + 1/2)\pi$  between the resonance curves of modes  $n^-$  and  $(n + 1)^+$ , i.e.  $\bar{\vartheta}_{n^-} = \bar{\vartheta}_{(n+1)^+}$ , from which

$$|\arg(\lambda)| = \pi/2,$$

so that the eigenvalues  $\lambda_i$  must be both imaginary. From (4),

$$t = \frac{\lambda^2 + d}{2\lambda}$$

follows; this shows that also  $t$  must be imaginary, which happens (see (7)) for

$$\Psi = \arctan v \pm \frac{\pi}{2} = \arctan \left( \frac{\tan(\Delta\vartheta/2)}{\cos 2\Phi} \right) \pm \frac{\pi}{2}, \quad (18)$$

from which

$$\Delta\vartheta = -2 \arctan \left( \frac{\cos 2\Phi}{\tan \Psi} \right), \quad (19)$$

providing the position of the crossing point in the  $(\bar{\vartheta}, \Delta\vartheta)$  plane. Moreover, [12, eq. (25)] shows that in this condition  $\bar{\vartheta}_{z,21} = \pi/2$ , proving that in crossing points 100% reflectivity occurs. This is an important result of this work. For what concerns the zeros of the reflection coefficient, they are real or complex depending on  $\Delta\vartheta$ .

By using (5), (7) and (18) we obtain the following explicit expression of the eigenvalues in crossing points:

$$\lambda_X = -j\sqrt{1 - u^2} \sin^2 \frac{\Theta}{2} \pm j\sqrt{\cos^4 \frac{\Theta}{2} - u^2 \sin^4 \frac{\Theta}{2}}. \quad (20)$$

Figure 7 contains two sets of curves useful to perform a study of crossing conditions in the bimodal FPI parameter space. In fact, the solid and dashed curves are  $\Delta\vartheta$  and  $u$  contours, respectively, such that a crossing point occurs. The solid curves are obtained fixing  $\Delta\vartheta = \Delta\vartheta_i$  in (18). The dashed curves are determined by recalling the definition of  $u$  from (9)

$$u = \sin 2\Phi \cos \frac{\Delta\vartheta}{2} = \frac{\sin 2\Phi}{\sqrt{1 + \tan^2 \frac{\Delta\vartheta}{2}}}.$$

By eliminating  $\Delta\vartheta$  between this equation and (19), we find

$$\Psi = \text{atan} \frac{u \cos 2\Phi}{\sqrt{\sin^2 2\Phi - u^2}}, \quad (21)$$

which allows to draw the curves for a chosen  $u = u_i$ . As  $u$  increases from 0 to 1, the corresponding loops approach the horizontal line  $\Phi = \pi/4$ .

For all the gratings whose representative points lie on a  $\Delta\vartheta_i$  contour the eigenvalues  $\lambda(\Delta\vartheta_i)$  are imaginary, so they correspond to crossing points. From (20) it is clear that the parameters  $\Phi$  and  $\Psi$  influence the eigenvalues only through  $u$ . For this reason, on the  $u = u_i$  contours the eigenvalues are constant (and imaginary).

#### B. Anticrossing regions

The interest in anticrossing regions is related to the guidelines reported in [10], which suggest to design the high- $Q$  HCG resonator in their proximity. However, their presence is not a general property of bimodal FPIs, as shown in the example of Fig. 5(right), where only crossing points appear. There, in addition to the ‘‘usual’’ crossings (satisfying (18)), a second family appears, defined by the intersection of the resonance curves  $n^-$  and  $n^+$  or  $n^-$  and  $(n + 2)^+$ , i.e.  $\bar{\vartheta}_{n^-} = \bar{\vartheta}_{n^+}$  or  $\bar{\vartheta}_{n^-} = \bar{\vartheta}_{(n+2)^+}$ . It follows that

$$|\arg(\lambda)| = 0, \pi,$$

so that the eigenvalues  $\lambda_i$  must be both real, and the resulting crossing points will be located in  $\bar{\vartheta} = n\pi$ . From (5), it is clear that the  $\{\lambda_i\}$  are real if the half-trace ( $t$ ) is real and the discriminant ( $t^2 - d$ ) is positive. The condition of real trace is, recalling (7),

$$\Delta\vartheta = 2 \arctan(\tan \Psi \cos 2\Phi). \quad (22)$$

The constraint on the discriminant can be expressed as  $\Theta > \Theta_c$  (see (10)). This condition corresponds to the example in Fig. 6(right): since the  $\{\lambda_i\}$  trace close curves around the origin and have opposite phases because their product is real ( $\cos \Theta$ ), the eigenvalues can be both real. It is to be remarked that (22) causes the zero of  $S_{21}$  to be in  $\bar{\vartheta} = \{0, \pi\}$  (see [12, eq. (25)]), which means that also these “new” crossing points exhibit 100% reflectivity.

Anticrossing regions appear when the condition on the discriminant is not satisfied. This is geometrically evident from Fig. 6(left), where the eigenvalues are never real, and the resonance curves approach each other but do not cross. When (22) is satisfied the  $\{\lambda_i\}$  are complex conjugate, so they have the same magnitude ( $\sqrt{\cos \Theta}$ ). The resonance curves have the closest approach when  $|\arg \lambda_i|$  is minimum. As Fig. 6(left) clearly shows, in this case  $|\lambda_1| \neq |\lambda_2|$ , so the point of closest approach is different from it. This is shown in Fig. 5(left) by the blue dashed lines based on (22).

### C. Position and quality factor of Fano resonances

One of the most remarkable features of bimodal FPIs is the presence of Fano resonances in their response, *i.e.* very quick zero-one transitions, see for example [12, Fig. 5]. Their origin can be understood from Fig. 5; in the neighborhood of  $\Delta\vartheta = \pi$ , for example, the transmission and reflection zero loci are very close and intersect in a point  $F$ . This property, which can be observed also in Fig. 4, is proved by a remarkable general relationship that can be found between the zeros of  $S_{11}$  and  $S_{21}$  as given in [12, eqs. (26), (25)]:

$$\cos(2\bar{\vartheta}_{z,11}) - (1 - u^2) \cos(2\bar{\vartheta}_{z,21}) = -\frac{3 + \cos 2\Theta}{4 \cos \Theta} u^2. \quad (23)$$

From (9), if  $\Delta\vartheta = \pi + \delta \rightarrow \pi$ ,

$$u \simeq -\frac{\delta}{2} \sin 2\Phi \rightarrow 0,$$

so that  $\bar{\vartheta}_{z,11} \rightarrow \bar{\vartheta}_{z,21} \rightarrow \pi/2 - \Psi$  (see [12, eq. (25)]). Actually the two curves are not just intersecting, but also tangent the point  $F = (\bar{\vartheta} = \pi/2 - \Psi, \Delta\vartheta = \pi)$ . In fact, it can be shown that the Taylor expansion of  $\bar{\vartheta}_{z,11} - \bar{\vartheta}_{z,21}$  from (23) starts with a  $\delta^2$  term.

The coincidence of the reflection and transmission zeros is a paradox, but we notice that also a resonance curve passes through  $F$ . Indeed, if we Taylor expand around  $\Delta\vartheta = \pi$  the expression of the greater magnitude eigenvalue from (5), (6), we find

$$\lambda_F \simeq \cos \frac{\delta}{2} \exp \left[ j \left( \frac{\pi}{2} - \Psi + \cos 2\Phi \tan \frac{\delta}{2} \right) \right]. \quad (24)$$

Recalling [12, eq. (14)], the pole corresponding to  $\lambda_F$  is

$$\bar{\vartheta}'_{\text{pF}} \simeq \underbrace{\left( n + \frac{1}{2} \right) \pi - \Psi + \cos 2\Phi \tan \frac{\delta}{2}}_{\bar{\vartheta}'_{\text{pF}}} - j \underbrace{\ln \cos \frac{\delta}{2}}_{\bar{\vartheta}''_{\text{pF}}}. \quad (25)$$

This means that if  $\delta \rightarrow 0$ ,  $\bar{\vartheta}'_{\text{pF}} \rightarrow \bar{\vartheta}_{z,21}$  and the pole is purely real; so, the resonance curve passes through  $F$  and a cancellation takes place between  $\bar{\vartheta}'_{\text{pF}}$ , the zero of  $S_{21}$  and one of the zeros of  $S_{11}$ . Hence the device behaves as a single-mode FPI.

From Fig. 5 it appears also that the resonance curve is tangent in  $F$  to the other two. In fact, from (17) and (24), the slope of the resonance curve in  $\Delta\vartheta = \pi$  is seen to be  $(\cos 2\Phi)/2$ , which equals the slope of  $\bar{\vartheta}_{z,21}$  (see [12, eq. (25)]). This relevant property is at the basis of the existence of Fano resonances over a rather wide range of  $\Delta\vartheta$  values.

A very important figure of merit for a resonator is its quality factor  $Q$ , which we compute from  $Q = \omega'_p / (2\omega''_p)$ , where  $\omega_p = \omega'_p + j\omega''_p$  is the complex cavity pole [16]. Exploiting (25), we can then write the explicit expression of the quality factor for the higher  $Q$  mode:

$$Q = \frac{\bar{\vartheta}'_{\text{pF}}}{2\bar{\vartheta}''_{\text{pF}}} \simeq -\frac{(n + 1/2)\pi - \Psi + \cos 2\Phi \tan(\delta/2)}{2 \ln \cos(\delta/2)}.$$

As it could be expected, if  $\delta \rightarrow 0$ ,  $Q \rightarrow \infty$ .

### D. Resonances and leaky waves

The phenomena of total transmission and reflection in gratings has been explained in the past in terms of leaky waves [17]-[20]. The scattering matrix of the grating is in general a function of the frequency  $\omega$  and of the  $x$  component  $\xi$  of the wavevector of the incident plane wave. Leaky waves, also called quasimodes [21], are resonances associated to complex poles located on the line  $\{\omega_p, \xi_p = \xi(\omega_p)\}$  of the complex  $(\omega, \xi)$  plane, which crosses both the  $\Re\{\omega\}$  and  $\Re\{\xi\}$  axes. If one focuses on the concept of propagating wave,  $\omega_p$  is assumed real and  $\xi_p$  is complex: the real part is associated to the phase velocity of the wave along the grating surface and the imaginary part accounts for the radiation of energy via the non evanescent grating orders. On the contrary, if one stresses the oscillatory character of the field,  $\xi_p$  is assumed to be real and the corresponding frequency  $\omega_p = \omega(\xi_p)$  turns out to be complex, describing a damped oscillation. The latter point of view is implicitly adopted in the present approach, where the variable  $\bar{\vartheta}$  is used in place of the frequency  $\omega$ . Therefore our work is perfectly coherent with the leaky wave perspective, and adds physical insight by making explicit the relationship with reflection and transmission zeros.

## IV. LOW-CONTRAST GRATING RESONATORS

Inspired by Fig. 5(right), we looked for a dielectric grating with these characteristics. Since  $\Theta$  is fairly large, *i.e.* air-bar junctions should have low reflectivity, a simulation of  $\text{SiO}_2$  bars ( $n_1 = 1.45$ ) in air and  $\eta = 60\%$  was performed by means

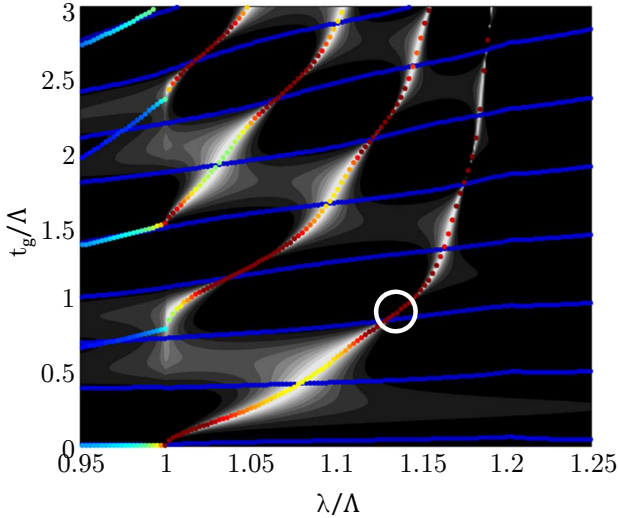


Fig. 8. TE reflectivity map for normal-incident plane-wave (linear, gray scale: brighter regions indicate high reflectivity) of a low-contrast grating in the  $(\lambda, t_g)$  plane. The grating consists of  $\text{SiO}_2$  bars ( $n_1 = 1.45$ ) surrounded by air,  $\eta = 60\%$ . The resonance curves are superimposed and their color quantifies the resonance quality factor (blue low, red high). The marker indicates the point  $U$  ( $\lambda = 1.141\Lambda$ ,  $t_g = 0.95\Lambda$ ), where  $Q \rightarrow \infty$ .

of the RCWA. This results in a low-contrast grating (LCG), which could be advantageous for technological reasons.

Maps similar to those of Figs. 2 and 3 are shown in Figs. 8 and 9. In order to characterize this structure, the parametric model is applied to the operation point  $U$  marked in the two figures, corresponding to  $\lambda = 1.141\Lambda$ ,  $t_g = 0.95\Lambda$ , where the quality factor is very high. The resulting parameters are  $\Theta = 84.35^\circ$ ,  $\Phi = 19.04^\circ$ ,  $\Psi = 254.52^\circ$ ,  $\Delta\vartheta = -180.07^\circ$ . It can be noted that this  $\Theta$  is similar to that of Fig. 6(right), exhibiting eigenvalue loci in the form of two concentric curves. This is a distinguishing feature of LCGs. Compared to Fig. 7, the area delimited by the thick red curve is smaller, as a consequence of the increased  $\Theta$ . It can be noted that the marker is out of this area, in accordance with the absence of anticrossing states in the reflectivity maps.

Since the dielectric contrast is much lower than in the structure considered in Section II, the new maps (drawn with the same color scale) are generally darker, and the dual-mode region is narrower. For these reasons, LCGs are not suitable for the implementation of broad-band reflectors. However, 100% reflectivity still occurs at crossing points; such narrow-band reflectors could be exploited for example in vertical-cavity surface-emitting lasers for spectrometry applications, to detect specific absorption lines.

The aforementioned high- $Q$  regions appear in the neighborhood of  $\Delta\vartheta = (2n + 1)\pi$ , as in HCGs. These features can be also observed in Fig. 10(right). It can be noted that  $\bar{\vartheta}_{z,21}$  and the resonance curves are almost superimposed. This is reasonable because these lines intersect in crossing and anticrossing points, they share the tangency point  $F$  and, for this device, they are almost straight.

However, it is to be remarked that if  $\Theta < \Theta_c$  as in Fig. 5(left), the resonance curves appear to be also very close to the  $\vartheta_{z,11}$  curves. The reason is that they have the common

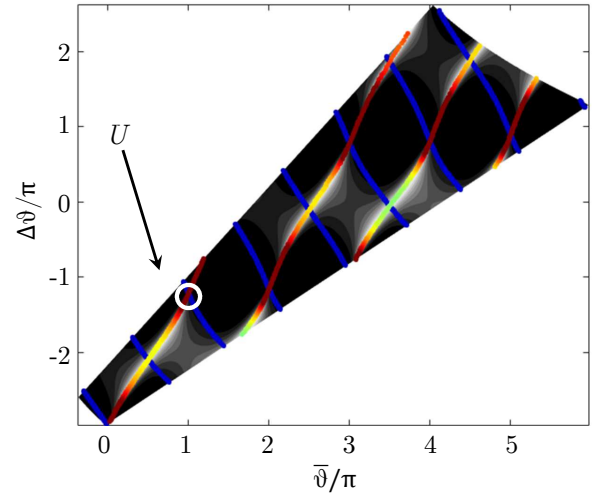


Fig. 9. Same reflectivity map of Figure 8, redrawn in the  $(\bar{\vartheta}, \Delta\vartheta)$  plane with reference to the dual-mode region  $\lambda \in [1, 1.15]\Lambda$ . The marker indicates the image of the point  $U$  of Fig. 8.

tangency point  $F$  and the  $\Delta\vartheta$  range of complex  $S_{11}$  zeros tends to vanish for decreasing  $\Theta$ . In conclusion, if  $\Theta$  and  $\Psi$  are small, the three curves are almost coincident.

From Figs. 8, 9 it appears clearly that only one of the eigenvalues exhibits a high quality factor. This can be explained looking at Fig. 6(right), related to Fig. 5(right): when  $\Theta > \Theta_c$  the two eigenvalues trace concentric curves, whose size is getting more different with increasing  $\Theta$ , see (5) with  $d = \cos\Theta$  small.

Figure 11 shows the reflectivity spectra of LCGs having thickness  $t_g = 0.9\Lambda$  (blue),  $t_g = 0.95\Lambda$  (red),  $t_g = \Lambda$  (orange). The relevant  $(\bar{\vartheta}, \Delta\vartheta)$  loci are reported in Fig. 10(right), with corresponding colors. The top axis reports the  $\bar{\vartheta}$  values corresponding to the peaks. The sharpest resonance corresponds obviously to  $\Delta\vartheta = -180.07^\circ$ , that is the point  $U$  indicated in Fig. 8. It should be noted that the corresponding cut in Fig. 10(right) intersects the tangency point among the three curves. As highlighted from the zoom, a very quick zero-one transition occurs, coherently with  $Q \rightarrow \infty$ . The orange curve exhibits a Fano resonance as well, but with much lower quality factor. Instead, the blue curve shows just a reflectivity peak, because of the asymmetric relative position between the resonance curves and the transmission/reflection zero loci: the reflection zero is so far that it is no longer possible to classify this behavior as a Fano resonance.

## V. CONCLUSION AND OUTLOOK

In this paper a novel framework for HCG/LCG resonators is proposed. Starting from a real device, the approach introduced in Part I is applied to reproduce the results obtained with a full-wave simulator, obtaining a good agreement. From the explicit formulas of the loop gain eigenvalues -and of their corresponding resonance curves- it is possible to predict, rather than just to observe, the position of crossing states, proving rigorously that they are 100% reflectivity points. Anticrossing states are fully characterized as well, showing that they are a degeneration of a second family of crossing

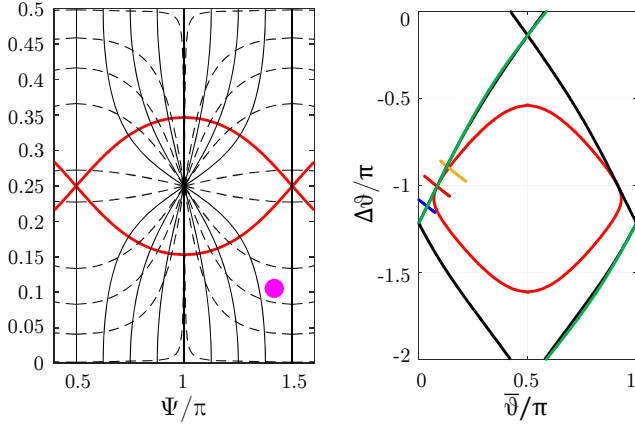


Fig. 10. Left: representation of the parameter plane ( $\Psi, \Phi$ ) for the low-contrast grating, as in Fig. 7. The marker indicates the point  $U$  of Fig. 8. Right: curves representing the loci of the transmission zeros  $\bar{\vartheta}_{z,21}$  (green), of the real reflection zeros  $\bar{\vartheta}_{z,11}$  (red), and the resonance curves (black), with the relevant mode indexes, as in Fig. 5. The junction parameters are:  $\Theta = 84.35^\circ$ ,  $\Phi = 19.04^\circ$ ,  $\Psi = 254.52^\circ$ . The three  $(\bar{\vartheta}, \Delta\theta)$  curves in the neighborhood of  $\Delta\theta/\pi = -1$  are those traced by the wavelength sweeps of Fig. 11, with corresponding colors.

points, defined here for the first time. These studies allowed us to propose for the first time LCGs as narrow-band mirrors and high- $Q$  resonators. The  $Q$  factor is provided by explicit formulas from the response poles, strictly related to the loop gain eigenvalues. An important result of this work is the quantification of the relationship between resonance curves and the transmission/reflection zeros loci, proving that Fano resonances degenerate into a zero-pole cancellation, disappearing from the response for  $\Delta\theta = \pi$ . This is in full agreement and quantifies the observations reported by Connie Chang-Hasnain *et al.* in [10].

This characterization of HCGs will be continued in a forthcoming work, which will deal with their broadband reflection features.

## REFERENCES

- [1] J. Niehusmann, A. Vörckel, P. Haring Bolivar, T. Wahlbrink, W. Henschel, and H. Kurz, "Ultra-high-quality-factor silicon-on-insulator microring resonator," *Opt. Lett.*, vol. 29, no. 24, pp. 2861-2863, Dec. 2004.
- [2] T. Asano, B.-S. Song, Y. Akahane, and S. Noda, "Ultra-high- $Q$  nanocavities in two-dimensional photonic crystal slabs," *J. Sel. Topics Quantum Electron.*, vol. 12, no. 6, pp. 1123-1134, Nov./Dec. 2006.
- [3] N. Rassem, A.-L. Fehrembach, and E. Popov, "Waveguide mode in the box with an extraordinary flat dispersion curve," *J. Opt. Soc. Am. A*, vol. 32, no. 3, pp. 420-430, Mar. 2015.
- [4] J. Inoue, K. Hatanaka, K. Kintaka, K. Nishio, and S. Ura, "Lens-less coupling of cavity-resonator-integrated guided-mode resonance filter," *J. Lightw. Technol.*, vol. 33, no. 24, pp. 5278-5283, Dec. 2015.
- [5] C. F. R. Mateus, M. C. Y. Huang, Y. Deng, A. R. Neureuther, and C. J. Chang-Hasnain, "Ultrabroadband mirror using low-index cladded subwavelength grating," *IEEE Photon. Technol. Lett.*, vol. 16, no. 2, pp. 518-520, Feb. 2004.
- [6] Y. Zhou, M. Moewe, J. Kern, M. C. Y. Huang, and C. J. Chang-Hasnain, "Surface-normal emission of a high- $Q$  resonator using a subwavelength high-contrast grating," *Opt. Express*, vol. 16, no. 22, pp. 17282-17287, Oct. 2008.
- [7] Y. Zhou, M. C. Y. Huang, C. Chase, V. Karagodsky, M. Moewe, B. Pesala, F. G. Sedgwick, and C. J. Chang-Hasnain, "High-index contrast grating (HCG) and its applications in optoelectronic devices," *J. Sel. Topics Quantum Electron.*, vol. 15, no. 5, pp. 1485-1499, Sept./Oct. 2009.

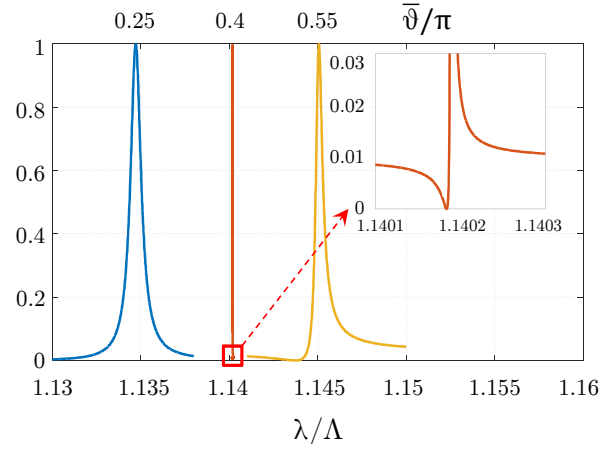


Fig. 11. Cuts of the reflectivity map reported in Fig. 8 for  $t_g = 0.9\Lambda$  (blue),  $t_g = 0.95\Lambda$  (red),  $t_g = \Lambda$  (orange). A zoom on the red curve is used to highlight its very quick zero-one transition. At top, the normalized  $\bar{\vartheta}$  values of the peaks are reported to establish the correspondence with Fig. 10.

- [8] V. Karagodsky and C. J. Chang-Hasnain, "Physics of near-wavelength high contrast gratings," *Opt. Express*, vol. 20, no. 10, pp. 10888-10895, May 2012.
- [9] V. Karagodsky, C. Chase, and C. J. Chang-Hasnain, "Matrix Fabry-Pérot resonance mechanism in high-contrast gratings," *Opt. Lett.*, vol. 36, no. 9, pp. 1704-1706, Apr. 2011.
- [10] C. J. Chang-Hasnain and W. Yang, "High-contrast gratings for integrated optoelectronics," *Adv. Opt. Photon.*, vol. 4, no. 3, pp. 379-440, 2012.
- [11] A. Taghizadeh, J. Mørk, and I.-S. Chung, "Ultracompact resonator with high quality-factor based on a hybrid grating structure," *Opt. Express*, vol. 23, no. 11, pp. 14913-14921, May 2015.
- [12] R. Orta, A. Tibaldi, and P. Debernardi, "Bimodal resonance phenomena. Part I: generalized Fabry-Pérot interferometers," *IEEE J. Quantum Electron.*, vol. xx, no. x, pp. xxx, xxx, xxx.
- [13] M. G. Moharam and T. K. Gaylord, "Rigorous coupled-wave analysis of planar-grating diffraction," *J. Opt. Soc. Am.*, vol. 71, no. 7, pp. 811-818, July 1981.
- [14] V. Karagodsky, F. G. Sedgwick, and C. J. Chang-Hasnain, "Theoretical analysis of subwavelength high contrast grating reflectors," *Opt. Express*, vol. 18, no. 16, pp. 16973-16988, Aug. 2010.
- [15] A. Tibaldi, P. Debernardi, and R. Orta, "High-contrast gratings performance issues in tunable VCSELs," *IEEE J. Quantum Electron.*, vol. 51, no. 12, pp. 2400407, Dec. 2015.
- [16] A. Taghizadeh, J. Mørk, and I.-S. Chung, "Comparison of different numerical methods for quality factor calculation of nano and micro photonic cavities," *Metamaterials'2014*, Copenhagen, 25-30 Aug. 2014.
- [17] H. L. Bertoni, L.-H. S. Cheo, and T. Tamir, "Frequency-selective reflection and transmission by a periodic dielectric layer," *IEEE Trans. Antennas Propag.*, vol. 37, no. 1, pp. 78-83, Jan. 1989.
- [18] K. M. Lee, P. T. Leung, and K. M. Pang, "Dyadic formulation of morphology-dependent resonances. I. Completeness relation," *J. Opt. Soc. Am. B*, vol. 16, no. 9, pp. 1409-1417, Sept. 1999.
- [19] S. Fan, W. Suh, and J. D. Joannopoulos, "Temporal coupled-mode theory for the Fano resonance in optical resonators," *J. Opt. Soc. Am. A*, vol. 20, no. 3, pp. 569-572, Mar. 2003.
- [20] J. Hu and C. R. Menyuk, "Understanding leaky modes: slab waveguide revisited," *Adv. Opt. Photon.*, vol. 1, no. 1, pp. 58-106, 2009.
- [21] B. Vial, F. Zolla, A. Nicolet, and M. Commandré, "Quasimodal expansion of electromagnetic fields in open two-dimensional structures," *Phys. Rev. A*, vol. 89, pp. 023829, Feb. 2014.

**The Authors' biographies can be found in Part I.**